

Thermal Analysis and Crystallization of Bioactive Glass "1d" in the SiO<sub>2</sub>-CaO-MgO-P<sub>2</sub>O<sub>5</sub>-CaF<sub>2</sub>-Na<sub>2</sub>O Compositional System

*Original*

Thermal Analysis and Crystallization of Bioactive Glass "1d" in the SiO<sub>2</sub>-CaO-MgO-P<sub>2</sub>O<sub>5</sub>-CaF<sub>2</sub>-Na<sub>2</sub>O Compositional System / Rigano, V.; Tulyaganov, D. U.; Dimitriadis, K.; Agathopoulos, S.; Baino, F.. - In: CERAMICS. - ISSN 2571-6131. - ELETTRONICO. - 8:4(2025), pp. 1-13. [10.3390/ceramics8040145]

*Availability:*

This version is available at: 11583/3011397 since: 2026-05-26T09:20:50Z

*Publisher:*

Multidisciplinary Digital Publishing Institute (MDPI)

*Published*

DOI:10.3390/ceramics8040145

*Terms of use:*

This article is made available under terms and conditions as specified in the corresponding bibliographic description in the repository

*Publisher copyright*

(Article begins on next page)

## Article

# Thermal Analysis and Crystallization of Bioactive Glass “1d” in the SiO<sub>2</sub>-CaO-MgO-P<sub>2</sub>O<sub>5</sub>-CaF<sub>2</sub>-Na<sub>2</sub>O Compositional System

Valentina Rigano <sup>1</sup>, Dilshat U. Tulyaganov <sup>2</sup>, Konstantinos Dimitriadis <sup>3</sup>, Simeon Agathopoulos <sup>4</sup>  
and Francesco Baino <sup>1,\*</sup>

<sup>1</sup> Institute of Materials Physics and Engineering, Department of Applied Science and Technology, Politecnico di Torino, 10129 Torino, Italy; valentina.rigano@polito.it

<sup>2</sup> Department of Natural-Mathematical Sciences, Turin Polytechnic University in Tashkent, Tashkent 100095, Uzbekistan; tulyaganovdilshat@gmail.com

<sup>3</sup> Division of Dental Technology, Department of Biomedical Sciences, University of West Attica, 12243 Athens, Greece; dimitriadiskonstantinos@hotmail.com

<sup>4</sup> Department of Materials Science and Engineering, School of Engineering, University of Ioannina, 45110 Ioannina, Greece; sagat@uoi.gr

\* Correspondence: francesco.baino@polito.it

## Abstract

The crystallization behavior of the bioactive silicate glass “1d” was analyzed using non-isothermal conditions through differential scanning calorimetry (DSC). The plots carried out at different heating rates showed only one crystallization peak. The activation energy for crystallization was calculated through the equations proposed in the Kissinger and Matusita–Sakka models. The Johnson–Mehl–Avrami coefficient (n) was estimated by applying Ozawa and Augis–Bennet methods, resulting in a two-dimensional crystal growth. Crystalline phases which developed during high-temperature treatment were analyzed by X-ray diffraction and scanning electron microscopy. The activation energy for viscous flow was estimated to be 513 kJ/mol, which is lower than the activation energy for crystallization (539 kJ/mol). The Malek test highlighted that the crystallization process was more complex than a simple nucleation-growth mechanism. The sinterability parameter and Hruby coefficient showed the high stability of 1d glass against crystallization, which makes this bioactive material highly appealing for producing well-sintered products of biomedical interest, such as bioactive porous scaffolds for bone regeneration.

**Keywords:** bioactive glass; glass-ceramic; thermal analysis; crystallization



Academic Editors: Gilbert Fantozzi and Vincent Garnier

Received: 15 October 2025

Revised: 22 November 2025

Accepted: 24 November 2025

Published: 26 November 2025

**Citation:** Rigano, V.; Tulyaganov, D.U.; Dimitriadis, K.; Agathopoulos, S.; Baino, F. Thermal Analysis and Crystallization of Bioactive Glass “1d” in the SiO<sub>2</sub>-CaO-MgO-P<sub>2</sub>O<sub>5</sub>-CaF<sub>2</sub>-Na<sub>2</sub>O Compositional System. *Ceramics* **2025**, *8*, 145. <https://doi.org/10.3390/ceramics8040145>

**Copyright:** © 2025 by the authors. Licensee MDPI, Basel, Switzerland. This article is an open access article distributed under the terms and conditions of the Creative Commons Attribution (CC BY) license (<https://creativecommons.org/licenses/by/4.0/>).

## 1. Introduction

The origin of bioactive glasses dates back to the years 1967–1969 at the University of Florida (USA), where a research team led by Prof. Larry Hench developed and characterized different glass compositions belonging to the SiO<sub>2</sub>-Na<sub>2</sub>O-CaO-P<sub>2</sub>O<sub>5</sub> quaternary system [1]. Specifically, the formulation 45SiO<sub>2</sub>-24.5Na<sub>2</sub>O-24.5CaO-6P<sub>2</sub>O<sub>5</sub> (wt.%), referred to as 45S5 and later trademarked as Bioglass<sup>®</sup>, was selected as the most promising one because of its easy melting and high CaO-to-P<sub>2</sub>O<sub>5</sub> ratio (similar to that found in the mineral phase of human bone), which allowed this biomaterial to be “surface-active” and react in a physiological environment with living tissues. Experiments carried out on 45S5 Bioglass<sup>®</sup> showed an excellent biocompatibility and capability to stimulate bone regeneration [2]. Many in vitro and in vivo tests were then performed on such a glass to prove its extraordinary ability to bond to bone through the formation of an interfacial layer of nano-crystalline

hydroxyapatite, as well as its potential to stimulate bone cells towards a path of high viability and osteogenesis [3]. Further studies revealed the ability of the 45S5 glass composition to bond to non-mineralized soft tissues, too, thereby broadening the horizons in tissue engineering applications [4,5].

Since then, many other bioactive glass systems have been designed, developed and characterized by scientists working in the field; these biomaterials are typically categorized in three main groups according to the main former oxide, i.e., SiO<sub>2</sub>-, B<sub>2</sub>O<sub>3</sub>- and P<sub>2</sub>O<sub>5</sub>-based bioactive glasses.

In silicate glasses, such as the well-known 45S5 Bioglass<sup>®</sup>, the amorphous network is formed by basic units of (SiO<sub>4</sub>)<sup>4-</sup> tetrahedra where each bridging oxygen is coordinated by two silicon cations (Si–O–Si), thus resulting in relatively open structures which can be easily disrupted upon contact with biological fluids.

In the late 1990s, borate and borosilicate glasses were first proposed for bone-repair applications [6]. Such glasses, being highly reactive in aqueous media, exhibit a lower chemical durability compared to silicate materials, yielding the faster formation of a surface layer of hydroxyapatite faster [7].

In the same period, phosphate glasses were also introduced as highly resorbable materials for biomedical applications [8]. In nature, the phosphate group (PO<sub>4</sub>)<sup>3-</sup> exists as a tetrahedral structural unit, which is intrinsically asymmetric. P–O–P bonds undergo easy hydration and thus promote the fast solubility of these glasses in biological fluids with kinetics ranging from hours to weeks, depending on the glass composition [9].

In general, the bioactivity mechanism relies on the dissolution of the amorphous fraction of glass upon contact with bio-fluids. However, during high-temperature post-processing treatments (e.g., sintering of glass particles, consolidation of coatings), bioactive glasses may undergo devitrification [10]. This involves the partial conversion of the glass into crystalline domains, yielding the development of glass–ceramic products. While this is beneficial from a mechanical viewpoint (e.g., improvement of hardness, strength and toughness which are key, for example, in dental applications [11]), on the other hand, the nucleation and growth of crystalline phases reduce the volume of the glassy fraction and, hence, the bioactivity. The nature of the crystalline phases that develop in the parent glass strongly depends on material composition. Heat-treated glasses based on the SiO<sub>2</sub>–CaO–Na<sub>2</sub>O system tend to typically form sodium–calcium–silicate phases: for example, 45S5 and S53P4 (53SiO<sub>2</sub>–23Na<sub>2</sub>O–20CaO–4P<sub>2</sub>O<sub>5</sub> wt.%) glasses devitrify at 550–600 °C into combeite-like phases (Na<sub>2</sub>CaSi<sub>2</sub>O<sub>6</sub> [12] and Na<sub>2</sub>Ca<sub>2</sub>Si<sub>3</sub>O<sub>9</sub> [13], respectively). Other bioactive glasses in the CaO–MgO–SiO<sub>2</sub> system form diopside (CaMgSi<sub>2</sub>O<sub>6</sub>) and wollastonite (CaSiO<sub>3</sub>) crystals [14].

With regard to the last class, the multicomponent bioactive glass “1d” (BG1d; composition 46.1SiO<sub>2</sub>–28.7CaO–8.8MgO–6.2P<sub>2</sub>O<sub>5</sub>–5.7CaF<sub>2</sub>–4.5Na<sub>2</sub>O wt.%) has attracted great attention by researchers over the last years; the genesis and application of this biomaterial have been comprehensively reviewed in a recent publication [15]. BG1d has a fast apatite-forming ability in simulated body fluid (SBF) [16] and exhibits good in vitro (cell culture) and in vivo performances (rabbit model), with low inflammatory cell infiltration and excellent biocompatibility [17]. A comparative study also showed that BG1d is associated with larger cell viability and proliferation compared to 45S5 Bioglass<sup>®</sup> used as a reference, which was probably due to the lower Na amount—yielding a milder pH rise and alkalinity in aqueous media—and the release of Mg ions exerting a stimulatory effect on osteoblasts [18]. BG1d particles were clinically used in 45 human volunteers for the treatment of jawbone defects after cystectomy operations, leading to complete bone regeneration at 2 postoperative months [15]. BG1d-derived porous scaffolds with trabecular architecture were produced by both the foam replica method [19] and additive manufac-

turing (vat photopolymerization) [20]. The mechanical properties and machinability of a set of BG1d-derived glass–ceramic products were investigated for potential use in dental applications [21,22].

The study of crystallization behavior is key to properly design the fabrication route and features of devitrified materials. In this regard, early results were reported by Dimitriadis et al. [23], who analyzed the sinter-crystallization of bulk samples as well as BG1d particles with a size of 32  $\mu\text{m}$ . However, a devitrification mechanism also depends on size effects, i.e., smaller glass particles yield a shift in the crystallization onset to lower temperatures [24]. In order to gain further knowledge on this matter, the present study aims at investigating the crystallization behavior of finer BG1d particles, which—for example—were recently used for producing 3D-printed porous scaffolds [25] that need to be consolidated through high-temperature thermal treatment.

## 2. Materials and Methods

### 2.1. Fabrication of Glass and Glass–Ceramics

Bioactive glass (BG1d) in the oxide composition of 46.1SiO<sub>2</sub>-28.7CaO-8.8MgO-6.2P<sub>2</sub>O<sub>5</sub>-5.7CaF<sub>2</sub>-4.5Na<sub>2</sub>O (wt %) was produced by melting at 1450 °C according to a procedure described elsewhere [26], cast in water, ball-milled using a planetary mill (Pulverisette 6, Fritsch, Idar-Oberstein, Germany) and eventually sifted below 25  $\mu\text{m}$ . This particle size was previously demonstrated by the authors to be suitable for producing bone-like porous scaffolds by additive manufacturing technologies [20]. Bulk glasses (free of crystalline inclusions, as verified by X-ray diffraction analysis) were fabricated by casting the molten material into preheated bronze molds, followed by an annealing process at 650 °C for 1 h. This annealing temperature was selected to be close to the glass transition temperature.

### 2.2. Thermal Analyses and Assessment of Crystallization Kinetics

In order to determine the thermal properties of the glass, differential scanning calorimetry (DSC 404 Netzsch, Netzsch, Selb, Germany) was performed on 25 mg of powder in a platinum crucible with four different heating rates  $\beta$  (10, 20, 30 and 40 °C/min) from room temperature to 1400 °C. Four characteristic temperatures of BG1d were assessed, i.e., glass transition ( $T_g$ ), crystallization onset ( $T_x$ ), crystallization peak ( $T_p$ ) and melting ( $T_m$ ).

The crystallization kinetics were evaluated using different approaches to determine the activation energy and identify the crystallization mechanism. The activation energy for the crystallization process was determined using non-isothermal conditions. The first approach adopted was the classical Kissinger method, which assumes a constant number of nuclei during transformations. Hence, the Kissinger equation is expressed as follows [27]:

$$\ln \frac{\beta}{T_p^2} = -\frac{E_{c,k}}{RT_p} + \text{constant} \quad (1)$$

where  $E_{c,k}$  is the apparent activation energy. A linear plot of  $\ln \frac{\beta}{T_p^2}$  vs.  $\frac{1}{T_p}$  yields a slope from which the activation energy can be extracted. However, this method assumes that nucleation is complete prior to crystal growth, which may not be valid for systems where nucleation continues during the thermal scan. In order to account for this and avoid underestimating the value of the activation energy, the more general Matusita–Sakka equation was then applied, modifying the previous model as follows [28]:

$$\ln \frac{\beta^n}{T_p^2} = -\frac{mE_c}{RT_p} + \text{constant} \quad (2)$$

where  $n$  is the Johnson–Mehl–Avrami (JMA) exponent and  $m$  is a factor that describes the dimensionality of crystal growth (ideally,  $m = 1$  means one-dimensional rod-like crystals,  $m = 2$  means two-dimensional plate-like crystals and  $m = 3$  means three-dimensional sphere-like crystals) [29]. When crystal nucleation occurs during the thermal program, we have  $m = n - 1$ . By plotting  $\ln \frac{\beta^n}{T_p^2}$  vs.  $\frac{1}{T_p}$ , the slope line gives  $-\frac{mE_C}{R}$ , from which the true activation energy can be calculated.

The activation energy associated with viscous flow ( $E_{vf}$ ) was evaluated using a Kissinger-type analysis [30]. This approach assumes that the temperature corresponding to the glass transition ( $T_g$ ) shifts with heating rate in a manner analogous to crystallization processes. The applied model involves plotting  $\ln \frac{\beta}{T_g^2}$  vs.  $\frac{1}{T_g}$ . The resulting linear relationship has a slope equal to  $-\frac{E_{vf}}{R}$ , from which the value of  $E_{vf}$  is directly calculated.

The JMA coefficient  $n$ , which may give information about the dimensionality of crystal growth, has been quantified first by applying the Ozawa equation [31]:

$$-n = \frac{d(\ln(-\ln(1 - \chi)))}{d(\ln \beta)} \quad (3)$$

where  $\chi$  denotes the fraction of material crystallized at a specific temperature. The values of  $\chi$  were derived from DSC thermograms, being calculated as the ratio of the area under the curve up to a chosen temperature and the total area under the exothermic peak. By plotting  $\ln(-\ln(1 - \chi))$  vs.  $\ln \beta$ , a linear trend was obtained with the slope of this line corresponding to the value of  $n$ . The final value of  $n$  was reported as the mean  $\pm$  standard deviation of the slopes of the different plots.

The second method used for determining  $n$  was the Augis–Bennet equation [32]:

$$n = \frac{2.5RT_p^2}{\Delta T_{FWHM}E_C} \quad (4)$$

where  $T_p$  is the peak temperature of crystallization,  $\Delta T_{FWHM}$  is the full width at half maximum of the exothermic peak,  $E_C$  is the activation energy and  $R$  is the universal gas constant ( $R = 8.314 \text{ J/mol K}$ ). For this approach, the value of  $n$  was computed individually for each heating rate and presented as mean  $\pm$  standard deviation.

As a final step, the validity of the JMA model in this specific study was discussed by applying the Malek test [33]. To ensure the applicability of the model, the crystallization rate  $d\chi$  should depend on the crystallized volume fraction  $\chi$  at the temperature  $T$ . This assumption can be tested using a probe function  $z(\chi) \propto d\chi$ , which, under non-isothermal conditions, is defined as follows:

$$z(\chi) = \Phi T^2 \quad (5)$$

where  $\Phi$  is the specific heat flow obtained from the DSC thermograms.

The JMA model is fully appropriate if the crystallization rate  $d\chi/dt$  depends only on the fraction  $\chi$  of crystallized material and the temperature  $T$  (i.e., in other words, the thermal history of the materials should not affect the crystallization mechanism). These conditions are verified—and hence the JMA model is valid—if the peak of  $z(\chi)$  occurs at  $\chi = 0.63 \pm 0.02$  [34].

### 2.3. Characterization of Samples

BG1d-derived glass–ceramic (GC1d) specimens were fabricated by compacting glass powders and subsequently subjecting these “green” bodies to a controlled sinter-crystallization process. BG1d fine powder (with particle size  $< 25 \mu\text{m}$ ) was mixed with 2.5 vol.% polyvinyl alcohol (PVA) solution (the glass powder/PVA weight ratio was 97.5:2.5). Parallelepiped samples ( $5 \times 4 \times 40 \text{ mm}^3$ ) were prepared by uniaxial press-

ing at about 200 bar. According to the results of the DSC analysis, the heat treatment of the samples (air atmosphere) comprised the following stages: (i) slow heating at 3 °C/min up to 450 °C with a dwell time of 2 h being applied for de-binding; (ii) further heating at 5 °C/min up to the “sintering window” temperature, with a dwell time of 30 min; (iii) finally, the bar was heated again at 5 °C/min up to the final temperature  $T_p$  with a dwell time of 1 h. Then, the specimens were left to slowly cool down to room temperature inside the furnace. The produced GC1d bars were rectified and their surfaces were polished (mirror finishing) using SiC papers (grid from 200 to 1200); finally, diamond pastes down to 1  $\mu\text{m}$  grain size were applied for ultrafine polishing (RotoPol-25, Struers, Ballerup, Denmark).

X-ray diffraction (XRD) analysis was employed to identify both the amorphous structure and the crystalline phases formed in the BG1d and GC1d samples, respectively. Measurements were conducted using a D8 Advance diffractometer (Bruker AXS, Billerica, MA, USA) with Cu K $\alpha$  radiation ( $\lambda = 1.5406 \text{ \AA}$ ), operating at 30 kV and 25 mA (in the range of diffraction angles ( $2\theta$ ) between 20 and 60° with a  $2\theta$  step of 0.02°/s). The obtained diffractograms were matched against reference patterns from the International Center for Diffraction Data (ICDD) database.

Morphological and microstructural analysis was carried out on both the annealed bulk and the sinter-crystallized specimen. The specimens were prepared by mirror polishing, finishing with 1  $\mu\text{m}$  of diamond paste, and final chemical etching in a 2 vol.% HF solution for 30 s. Observations were performed using a scanning electron microscope (SEM, model 6510 LV, JEOL, Freising, Germany) operating at 20 kV and equipped with an energy-dispersive X-ray spectroscopy (EDS) system for elemental assessment.

### 3. Results and Discussion

#### 3.1. Thermal Properties and Assessment of Crystallization Energy

Figure 1 shows the DSC graph at different heating rates  $\beta$ . Only one exothermic peak is visible in all the measurements; as also shown in Table 1, the values of  $T_g$ ,  $T_x$  and  $T_p$  increase as the heating rate increases from 10 °C/min to 40 °C/min, while the melting temperature remains constant (i.e., it is insensitive to the values of  $\beta$ ).

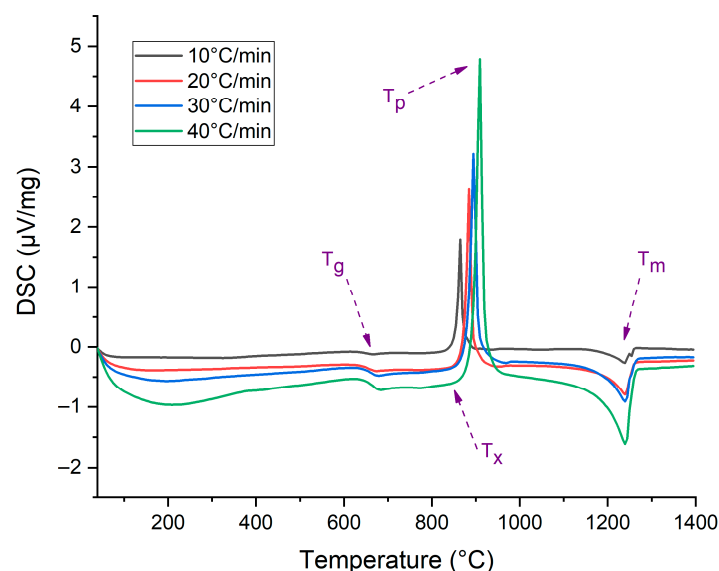


**Figure 1.** DSC thermographs at different heating rates; the characteristic temperatures were evaluated directly from the plots ( $T_g$  from the inflection point;  $T_x$  from the point at which the first derivative of the DCS curve becomes positive;  $T_p$  from the exothermic peaks;  $T_m$  from the endothermic peaks).

**Table 1.** Characteristic temperatures of BG1d.

$\beta$ ( $^{\circ}\text{C}/\text{min}$ )	$T_g$ ( $^{\circ}\text{C}$ )	$T_x$ ( $^{\circ}\text{C}$ )	$T_p$ ( $^{\circ}\text{C}$ )	$T_m$ ( $^{\circ}\text{C}$ )
10	647.9	836.0	864.9	1238.8
20	658.0	853.0	884.9	1240.1
30	663.3	860.0	895.4	1240.1
40	666.6	865.0	909.4	1240.7

In order to analyze the activation energy, the Kissinger equation has been used, finding an apparent activation energy  $E_{c,k}$  of 337 kJ/mol (Figure 2). However, this equation could lead to an underestimation of the energy. Considering that during the thermal measurement the number of nuclei is not constant, the dimensionality parameter  $m$  can be estimated as  $m = n - 1$ . The Avrami exponent  $n$  was determined from Ozawa plots (Figure 3) evaluated at different temperatures (880, 885, 890, 895 and 900  $^{\circ}\text{C}$ ), resulting in a value of  $2.85 \pm 0.62$  that reflects a 2D crystal growth. Knowing both  $n$  and  $m$ , the Matusita–Sakka equation was applied to provide a more accurate evaluation of the crystallization activation energy. The corresponding plot (Figure 4) yielded a significantly higher value of  $E_c = 539$  kJ/mol.

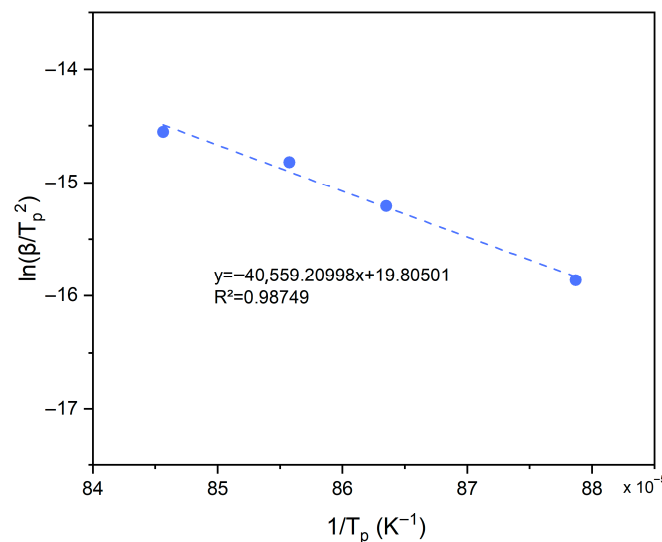


**Figure 2.** Linearized plot of the Kissinger equation (Equation (1)) to determine the apparent activation energy for crystallization ( $E_{c,k}$ ).

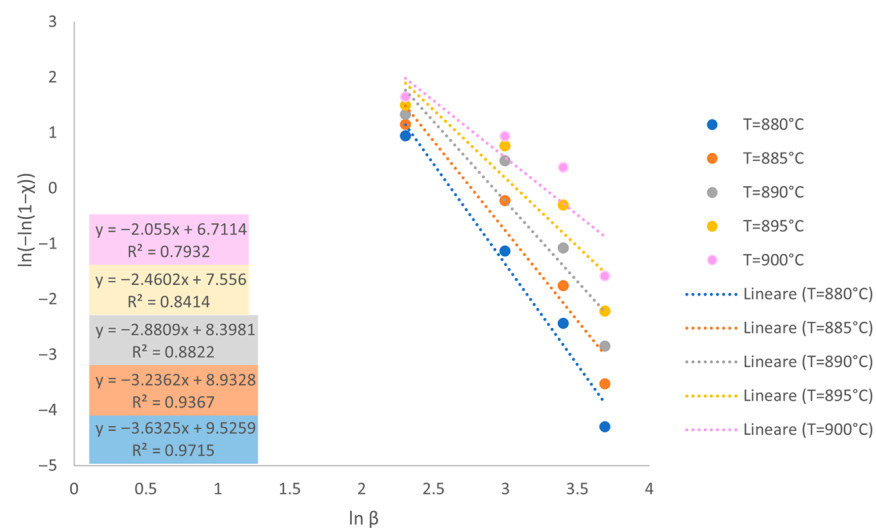


**Figure 3.** Linearized plot of the Ozawa equation (Equation (3)) to determine the JMA parameter ( $n$ ).

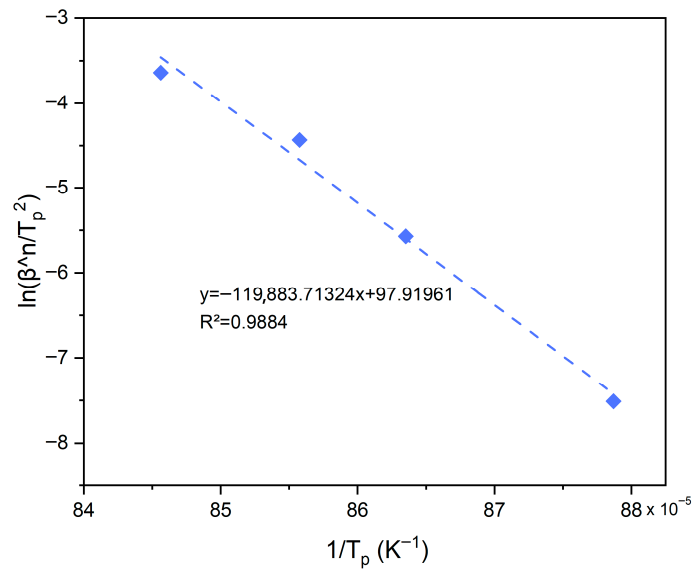


**Figure 4.** Linearized plot of the Matusita and Sakka equation (Equation (2)) to determine the correct activation energy for crystallization ( $E_c$ ).

### 3.2. Sintering Ability Against Crystallization

The Kissinger-type plot used to evaluate the activation energy for viscous flow ( $E_{vf}$ ) is presented in Figure 5, and the linear fit yielded a value of approximately 513 kJ/mol. The lower value of  $E_{vf}$  compared to  $E_c$  indicates that the energy barrier required for viscous flow to take place is smaller than that needed for diffusion to drive crystallization in BG1d.

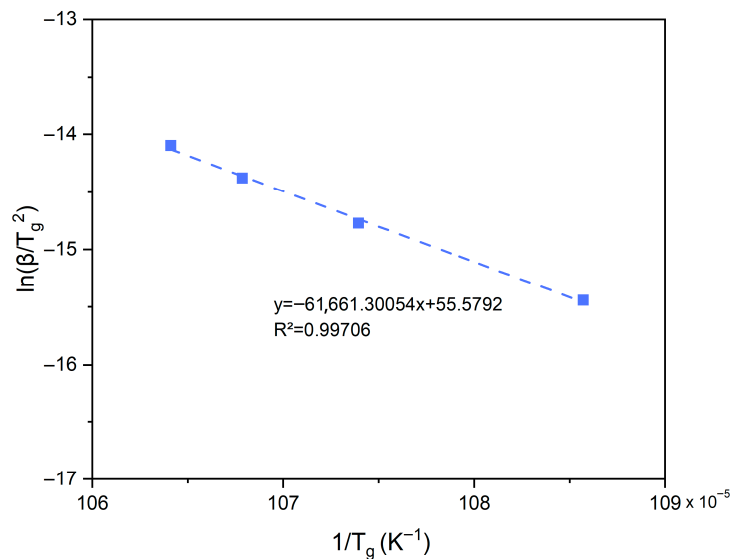


**Figure 5.** Kissinger-type plot for determining the activation energy for the viscous flow ( $E_{vf}$ ).

To further elucidate the relationship between sintering and crystallization in BG1d particles, a few additional thermal parameters were calculated. The difference between the onset of crystallization and the glass transition temperature, called “sintering window” and denoted as  $\Delta T = T_x - T_g$ , provides a common indicator of the glass resistance to crystallization. The larger this value, the higher the stability and the more reduced the tendency for rapid crystallization of a given glass upon heating. In the case of BG1d, this difference is not very sensitive to the value of  $\beta$  and ranges from 181.1 °C (heating rate 10 °C/min) to 198.4 °C (heating rate 40 °C/min).

A parameter called “sinterability”,  $S_c = T_x - T_{MS}$  [35], was also proposed in order to evaluate the kinetic competition between densification and crystallization during heating.

Here,  $T_{MS} = 768.4$  °C represents the temperature of maximum shrinkage, determined via hot-stage microscopy performed with a heating rate of 10 °C/min. For the BG1d particles investigated in the present work,  $S_c$  is around 67 °C (well above zero), suggesting that sintering can proceed independently of crystallization. In other words, sintering takes place before the onset of crystallization, favoring high densification of the glass before significant crystal growth, which is essential for fabricating mechanically strong glass-based products like porous scaffolds. For comparative purposes, the sinterability of 45S5 Bioglass® was assessed to be a negative value (<0) for melt-quenched particles sieved below 32 µm as well as commercial powder around 5 µm [24], meaning that sintering and crystallization are concurrent phenomena in this material regardless of particle size.

Additionally, the Hruby parameter,  $K_H$ , was further calculated as follows [36]:

$$K_H = \frac{T_x - T_g}{T_m - T_x} \quad (6)$$

using the characteristic temperatures reported in Table 1 for the different heating rates  $\beta$ . This parameter is used to measure the resistance of the material to devitrification—it is conceptually similar to  $S_c$ : higher values mean higher stability of the material in the glassy state, improved thermal stability and vitrifiability.

The values of  $K_H$  obtained for BG1d range from 0.467 (heating rate 10 °C/min) to 0.528 (heating rate 40 °C/min); the value determined with a heating rate of 10 °C/min is significantly higher than that reported for 45S5 Bioglass® (particle size < 32 µm) under the same experimental conditions ( $K_H = 0.066$  [37]), underscoring the superior thermal stability of the former over the reference benchmark.

Collectively, these parameters offer a valuable insight for optimizing the thermal treatment of BG1d, demonstrating its well-balanced thermal profile, offering both sintering efficiency and resistance to uncontrolled crystallization during heat processing.

### 3.3. Discussion of Model Applicability

To validate the calculated value of the Avrami coefficient, the Augis–Bennet method was also employed, which, however, yielded a much higher value of  $n$  ( $8.13 \pm 1.35$ ). This value is significantly higher than that reported by Dimitriadis et al. for larger BG1d particles (32 µm) analyzed by the same method [23]. In this regard, previous studies showed that the value of  $n$  obtained from the Augis–Bennett approach is often higher than the one derived from the Ozawa method because each technique is based on different assumptions about the crystallization mechanism, especially regarding nucleation behavior and crystal growth. In some cases, the Augis–Bennett method yields larger Avrami exponent values, which relate to the dimensional characteristics of crystal growth. The discrepancy between the two methods is not an indication of error; rather, it reflects their distinct theoretical backgrounds and the different ways they process the same non-isothermal data [38,39]. Therefore, a higher value of  $n$  from the Augis–Bennett method may suggest an alternative interpretation of the crystallization process, such as more extensive volumetric growth or an increase in homogeneous nucleation activity [40,41].

A value of  $n$  exceeding 4 (and, thus,  $m > 3$ ) is often considered to reveal a complex crystallization process, which is most probably surface-initiated [42]. This is consistent with the small size of BG1d particles used in the present work (<25 µm), also considering that using a small particle size often leads to surface crystallization even for glasses which would otherwise crystallize within the bulk [43]. This can be attributed to the very large surface area associated with fine particles, demonstrating the key role played by “dimensional effects”. Similar discrepancies in the values of  $n$  calculated through the Ozawa or Augis–Bennet methods were also reported by Massera et al. [38], who studied the crystallization

of phosphate glass particles and further confirmed that the value of  $n$  increased with decreasing glass particle size.

Indeed, the influence of the “size parameter” on the crystallization dimensionality may lead one to question the validity of the JMA model for BG1d compositions. For this purpose, the applicability of the JMA model was assessed using the equation and test proposed by Malek. The normalized function  $z(\chi)$  shows a typical bell-shaped profile (Figure 6), but the peak position was found to be around  $0.55 \pm 0.02$ , indicating that the JMA model may only approximately describe the crystallization mechanism of BG1d. Taken together, the result of the Malek test and the discrepancy in the  $n$  values determined through the Ozawa and Augis–Bennet methods suggest that the crystallization mechanism of BG1d changes as a function of the heating rate  $\beta$  and the particle size (as from the comparison with a previous study [23], where  $n = 3.8$  was found for BG1d particles around  $32 \mu\text{m}$ ), and it is more complex than a simple nucleation and growth process. This is consistent with previous observations on polished cross-sections of BG1d-derived samples that were thermally treated at different temperatures, revealing that liquid phase separations could be directly involved in the nucleation and crystal-growth processes [44].

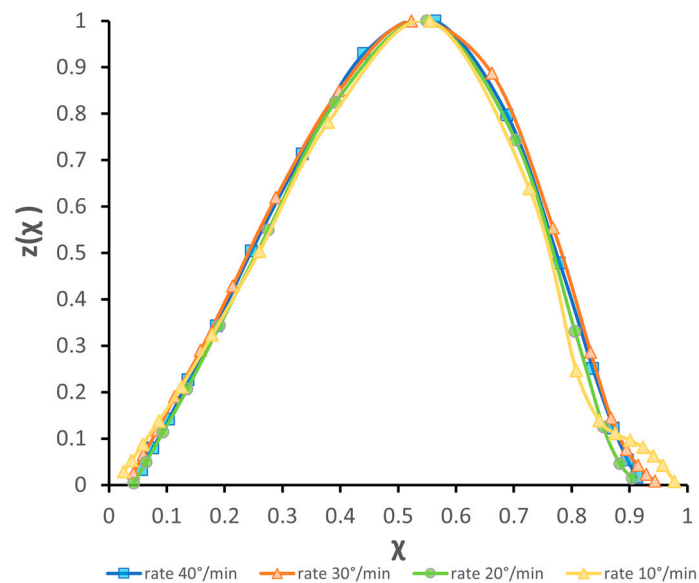


**Figure 6.** Normalized  $z(\chi)$  function (Malek test).

### 3.4. Glass–Ceramic 1d (GC1d) Through Devitrification of BG1d

In addition to the glass composition and thermal treatment (as previously discussed), the glass structure plays a critical role in guiding the crystallization pathway, ultimately determining the quality of the resulting GC. In other words, the crystallization of the glasses is stimulated by the glass structure, since liquid phase separation is directly involved in the development of crystalline phases through nucleation and the crystal growth [14,32]. Thus, studying the structure of glass is essential.

As mentioned in Section 2.1, the investigated BG1d were fully melted after 1 h at  $1450 \text{ }^\circ\text{C}$ . The molten material exhibited good castability, resulting in transparent and colorless glass without any visible crystalline inclusions or trapped air bubbles in the bulk. XRD analysis confirmed the amorphous nature of the produced annealed glass (Figure 7A). A representative SEM image of the chemically etched surface of the annealed bulk glass specimen is shown in Figure 7B, demonstrating that the BG1d is dense and free from defects. Furthermore, chemical etching revealed the presence of liquid–liquid phase separation within BG1d. Two distinct morphologies of phase-separated regions are visible: the bigger ones, marked with (i), which have an oval shape, and the tiny spots, indicated

by (ii). Nuclear magnetic resonance (NMR) studies performed previously on this glass system [26] demonstrated that the peaks of the  $^{29}\text{Si}$  NMR spectrum were associated with the dominance of  $Q^2$  (Si) structural units with the peak maximum at  $-76$  ppm, while the  $^{31}\text{P}$  NMR spectrum revealed the maximum peak position at 2.7 ppm, thus implying the formation of calcium orthophosphate groups. This phenomenon caused the formation of two distinct glassy phases, and the interfaces between the two separated glassy phases created sites for heterogeneous nucleation.

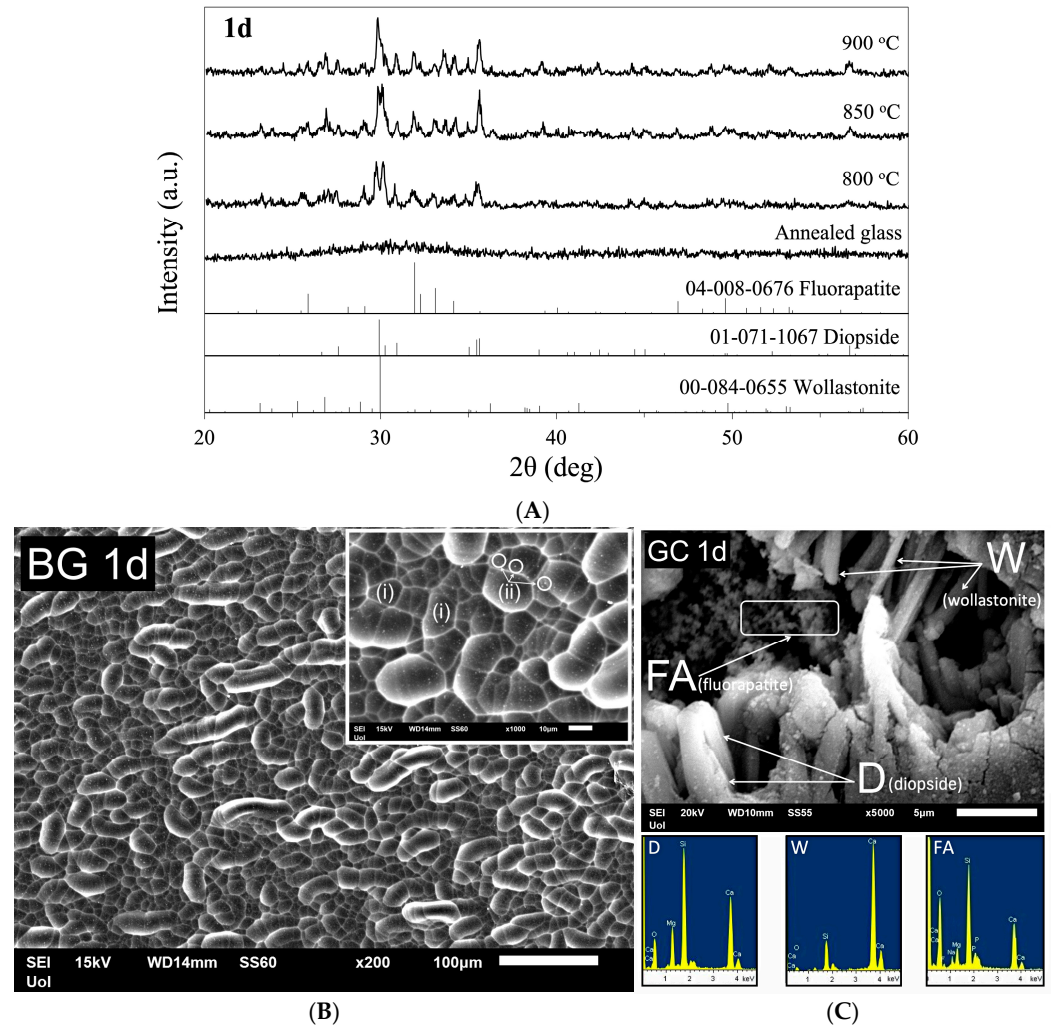


**Figure 7.** (A) X-ray diffractograms of annealed BG1d at 650 °C and sintered BG1d at 800 °C, 850 °C and 900 °C (GC1d samples). (B) Phase separation in annealed bulk BG1d (650 °C) and (C) microstructure and EDS of GC1d (850 °C) with the details of diopside (D), wollastonite (W) and fluorapatite (FA) crystals (the high peak for Si in the EDS analysis of FA phase is due to “border effects” associated with the surrounding crystalline species).

The heat treatment process of BG1d (based on the result of thermal analysis (DSC)) led to full dense GC. As shown in Figure 7A, the GC1d encompasses three crystalline phases, i.e., diopside ( $\text{CaMgSi}_2\text{O}_6$ ), wollastonite ( $\text{CaSiO}_3$ ) and fluorapatite ( $\text{Ca}_{10}(\text{PO}_4)_6\text{F}_2$ ). These crystals, embedded in a glassy matrix, were also observed (and identified by EDS elemental analysis) in the microstructure of the produced GCs. More specifically, the microstructure of the GC1d is mostly composed of relatively large prismatic diopside crystals and smaller acicular wollastonite crystals. Flake-like crystals were assigned to the fluorapatite phase (Figure 7C), which is formed due to the stronger electrostatic affinity of  $\text{Ca}^{2+}$  cations for coordinating with the more highly charged orthophosphate anions compared to non-

bridging oxygens in the silicate network. In turn,  $\text{CaF}_2$  forms mixed calcium fluoride species that are favorable for fluorapatite precipitation. Previous quantitative XRD studies based on Rietveld analysis for a GC1d powder compact sintered at 825 °C for 1 h [26] also allowed estimation of the amounts of phases in the glass–ceramic (diopside 44.60 wt.%, wollastonite 16.07 wt.%, fluorapatite 16.94 wt.% and residual glassy phase 22.39 wt.%). The peak intensities of XRD diffractograms in Figure 7A reveal that diopside crystallized as the major phase, while wollastonite and fluorapatite appeared as the secondary crystalline phases.

In conclusion, considering the aforementioned points, it is evident that the formation of crystalline phases in GC1d—produced through the controlled heat treatment of the parent BG1d glass—is also closely related to the structural characteristics of the parent glass.

#### 4. Conclusions

This study investigates the thermal behavior and crystallization mechanism of a  $\text{SiO}_2$ - $\text{CaO}$ - $\text{MgO}$ - $\text{P}_2\text{O}_5$ - $\text{CaF}_2$ - $\text{Na}_2\text{O}$  bioactive glass (powder with size below 25  $\mu\text{m}$ ), referred to as “1d”, under non-isothermal conditions. The results suggest that a complex crystallization process takes place, being surface-initiated and dependent on the heating rate and particle size. Hence, the crystallization process cannot be fully described by the JMA model. The Matusita–Sakka approach provides a more reliable crystallization activation energy compared to Kissinger’s one, while the lower viscous flow energy indicates that densification can take place before crystallization. In other words, sintering and crystallization are non-concurrent phenomena in BG1d, which is also confirmed by other thermal parameters like the large sintering window (around 200 °C). The knowledge and study of the (i) chemical composition, (ii) thermal behavior and (iii) structure of BG1d is key for producing high-quality glass-derived products via controlled heat treatment, such as porous scaffolds for bone tissue engineering applications and dental implants.

**Author Contributions:** Conceptualization, V.R. and F.B.; methodology, V.R., K.D. and F.B.; validation, D.U.T., K.D. and S.A.; investigation, V.R., D.U.T., K.D., S.A. and F.B.; resources, F.B.; data curation, V.R.; writing—original draft preparation, V.R.; writing—review and editing, D.U.T., K.D., S.A. and F.B.; supervision, D.U.T., S.A. and F.B.; project administration, F.B.; funding acquisition, F.B. All authors have read and agreed to the published version of the manuscript.

**Funding:** This study was carried out within the project “Artificial Intelligence-based design of 3D PRINTed scaffolds for the repair of critical-sized BONE defects—I-PRINT-MY-BONE” funded by the European Union—Next Generation EU within the PRIN 2022 program (D.D. 104—2 February 2022 Ministero dell’Università e della Ricerca). This manuscript reflects only the authors’ views and opinions, and the Ministry cannot be considered responsible for them.

**Institutional Review Board Statement:** Not applicable.

**Informed Consent Statement:** Not applicable.

**Data Availability Statement:** Raw data will be available on request.

**Conflicts of Interest:** The authors declare no conflicts of interest.

#### References

1. Hench, L.L. The story of Bioglass®. *J. Mater. Sci. Mater. Med.* **2006**, *17*, 967–978. [[CrossRef](#)] [[PubMed](#)]
2. Wilson, J.; Pigott, G.H.; Schoen, F.J.; Hench, L.L. Toxicology and biocompatibility of bioglasses. *J. Biomed. Mater. Res.* **1981**, *15*, 805–817. [[CrossRef](#)] [[PubMed](#)]
3. Hench, L.L. Genetic design of bioactive glass. *J. Eur. Ceram. Soc.* **2009**, *29*, 1257–1265. [[CrossRef](#)]
4. Miguez-Pacheco, V.; Hench, L.L.; Boccacini, A.R. Bioactive glasses beyond bone and teeth: Emerging applications in contact with soft tissues. *Acta Biomater.* **2015**, *13*, 1–15. [[CrossRef](#)]
5. Kargozar, S.; Hamzehlou, S.; Baino, F. Potential of Bioactive Glasses for Cardiac and Pulmonary Tissue Engineering. *Materials* **2017**, *10*, 1429. [[CrossRef](#)]

6. Brink, M.; Turunen, T.; Happonen, R.P.; Yli-Urpo, A. Compositional dependence of bioactivity of glasses in the system  $\text{Na}_2\text{O}-\text{K}_2\text{O}-\text{MgO}-\text{CaO}-\text{B}_2\text{O}_3-\text{P}_2\text{O}_5-\text{SiO}_2$ . *J. Biomed. Mater. Res.* **1997**, *37*, 114–121. [CrossRef]
7. Abodunrin, O.D.; El Mabrouk, K.; Bricha, M. A review on borate bioactive glasses (BBG): Effect of doping elements, degradation, and applications. *J. Mater. Chem. B.* **2023**, *11*, 955. [CrossRef]
8. Andersson, O.H.; Liu, G.; Karlsson, K.H.; Niemi, L.; Miettinen, J.; Juhanoja, J. In vivo behaviour of glasses in the  $\text{SiO}_2-\text{Na}_2\text{O}-\text{CaO}-\text{P}_2\text{O}_5-\text{Al}_2\text{O}_3-\text{B}_2\text{O}_3$  system. *J. Mater. Sci. Mater. Med.* **1990**, *1*, 219–227. [CrossRef]
9. Knowles, J.C. Phosphate based glasses for biomedical applications. *J. Mater. Chem.* **2003**, *13*, 2395–2401. [CrossRef]
10. Montazerian, M.; Zanutto, E.D. History and trends of bioactive glass-ceramics. *J. Biomed. Mater. Res. A* **2016**, *104*, 1231–1249. [CrossRef]
11. Montazerian, M.; Baino, F.; Fiume, E.; Migneco, C.; Alaghmandfard, A.; Sedighi, O.; DeCeanne, A.V.; Wilkinson, C.J.; Mauro, J.C. Glass-ceramics in dentistry: Fundamentals, technologies, experimental techniques, applications, and open issues. *Prog. Mater. Sci.* **2023**, *132*, 101023. [CrossRef]
12. Lefebvre, L.; Gremillard, L.; Chevalier, J.; Zenati, R.; Bernache-Assolant, D. Sintering behaviour of 45S5 bioactive glass. *Acta Biomater.* **2008**, *4*, 1894–1903. [CrossRef] [PubMed]
13. The Sintering Range of Porous Bioactive Glasses. Available online: [https://www.researchgate.net/publication/233521778\\_The\\_Sintering\\_Range\\_of\\_Porous\\_Bioactive\\_Glasses](https://www.researchgate.net/publication/233521778_The_Sintering_Range_of_Porous_Bioactive_Glasses) (accessed on 25 August 2025).
14. Tulyaganov, D.U.; Agathopoulos, S.; Ventura, J.M.; Karakassides, M.A.; Fabrichnaya, O.; Ferreira, J.M.F. Synthesis of glass-ceramics in the  $\text{CaO}-\text{MgO}-\text{SiO}_2$  system with  $\text{B}_2\text{O}_3$ ,  $\text{P}_2\text{O}_5$ ,  $\text{Na}_2\text{O}$  and  $\text{CaF}_2$  additives. *J. Eur. Ceram. Soc.* **2006**, *26*, 1463–1471. [CrossRef]
15. Tulyaganov, D.U.; Agathopoulos, S.; Dimitriadis, K.; Fernandes, H.R.; Gabrieli, R.; Baino, F. The Story, Properties and Applications of Bioactive Glass ‘1d’: From Concept to Early Clinical Trials. *Inorganics* **2024**, *12*, 224. [CrossRef]
16. Tulyaganov, D.U.; Agathopoulos, S.; Valerio, P.; Balamurugan, A.; Saranti, A.; Karakassides, M.A.; Ferreira, J.M.F. Synthesis, bioactivity and preliminary biocompatibility studies of glasses in the system  $\text{CaO}-\text{MgO}-\text{SiO}_2-\text{Na}_2\text{O}-\text{P}_2\text{O}_5-\text{CaF}_2$ . *J. Mater. Sci. Mater. Med.* **2011**, *22*, 217–227. [CrossRef]
17. Tulyaganov, D.U.; Makhkamov, M.E.; Urazbaev, A.; Goel, A.; Ferreira, J.M.F. Synthesis, processing and characterization of a bioactive glass composition for bone regeneration. *Ceram. Int.* **2013**, *39*, 2519–2526. [CrossRef]
18. Schmitz, S.I.; Widholz, B.; Essers, C.; Becker, M.; Tulyaganov, D.; Moghaddam, A.; de Juan, I.G.; Westhauser, F. Superior biocompatibility and comparable osteoinductive properties: Sodium-reduced fluoride-containing bioactive glass belonging to the  $\text{CaO}-\text{MgO}-\text{SiO}_2$  system as a promising alternative to 45S5 bioactive glass. *Bioact. Mater.* **2020**, *5*, 55–65. [CrossRef]
19. Baino, F.; Tulyaganov, D.U.; Kahharov, Z.; Rahdar, A.; Verné, E. Foam-Replicated Diopside/Fluorapatite/Wollastonite-Based Glass-Ceramic Scaffolds. *Ceramics* **2022**, *5*, 120–130. [CrossRef]
20. Baino, F.; Gaido, F.; Gabrieli, R.; Alidoost, D.; Schiavi, A.; Mohammadi, M.; Schwentenwein, M.; Tulyaganov, D.; Verné, E. Vat photopolymerization of ultra-porous bioactive glass foams. *Open Ceram.* **2024**, *20*, 100690. [CrossRef]
21. Dimitriadis, K.; Vasilopoulos, K.C.; Vaimakis, T.C.; Karakassides, M.A.; Tulyaganov, D.U.; Agathopoulos, S. Synthesis of glass-ceramics in the  $\text{Na}_2\text{O}/\text{K}_2\text{O}-\text{CaO}-\text{MgO}-\text{SiO}_2-\text{P}_2\text{O}_5-\text{CaF}_2$  system as candidate materials for dental applications. *Int. J. Appl. Ceram. Technol.* **2020**, *17*, 2025–2035. [CrossRef]
22. Dimitriadis, K.; Moschovas, D.; Tulyaganov, D.U.; Agathopoulos, S. Development of novel bioactive glass-ceramics in the  $\text{Na}_2\text{O}/\text{K}_2\text{O}-\text{CaO}-\text{MgO}-\text{SiO}_2-\text{P}_2\text{O}_5-\text{CaF}_2$  system. *J. Non-Cryst. Solids* **2020**, *533*, 119936. [CrossRef]
23. Dimitriadis, K.; Tulyaganov, D.U.; Vasilopoulos, K.C.; Karakassides, M.A.; Agathopoulos, S. Influence of K and Mg substitutions on the synthesis and the properties of  $\text{CaO}-\text{MgO}-\text{SiO}_2/\text{Na}_2\text{O}$ ,  $\text{P}_2\text{O}_5$ ,  $\text{CaF}_2$  bioactive glasses. *J. Non-Cryst. Solids* **2021**, *573*, 121140. [CrossRef]
24. Baino, F.; Fiume, E. Quantifying the effect of particle size on the crystallization of 45S5 bioactive glass. *Mater. Lett.* **2018**, *224*, 54–58. [CrossRef]
25. Schiavi, A.; Gaido, F.; Gabrieli, R.; Alidoost, D.; Schwentenwein, M.; Mohammadi, M.; Tulyaganov, D.; Verné, E.; Baino, F. Permeability and tomography-based microstructural analysis of ultra-porous bioactive glass scaffolds. *Mater. Lett.* **2025**, *384*, 138064. [CrossRef]
26. Kansal, I.; Tulyaganov, D.U.; Goel, A.; Pascual, M.J.; Ferreira, J.M.F. Structural analysis and thermal behavior of diopside-fluorapatite-wollastonite-based glasses and glass-ceramics. *Acta Biomater.* **2010**, *6*, 4380–4388. [CrossRef]
27. Kissinger, H.E. Variation of Peak Temperature with Heating Rate in Differential Thermal Analysis. *J. Res. Natl. Bur. Stand.* **1956**, *57*, 217. [CrossRef]
28. Matusita, K.; Sakka, S. Kinetic study of crystallization of glass by differential thermal analysis—Criterion on application of Kissinger plot. *J. Non-Cryst. Solids* **1980**, *38–39*, 741–746. [CrossRef]
29. Matusita, K.; Komatsu, T.; Yokota, R. Kinetics of non-isothermal crystallization process and activation energy for crystal growth in amorphous materials. *J. Mater. Sci.* **1984**, *19*, 291–296. [CrossRef]

30. Francis, A.A.; Rawlings, R.D.; Sweeney, R.; Boccaccini, A.R. Crystallization kinetic of glass particles prepared from a mixture of coal ash and soda-lime cullet glass. *J. Non Cryst. Solids* **2004**, *333*, 187–193. [[CrossRef](#)]
31. Ozawa, T. Kinetics of non-isothermal crystallization. *Polymer* **1971**, *12*, 150–158. [[CrossRef](#)]
32. Augis, J.A.; Bennett, J.E. Calculation of the Avrami parameters for heterogeneous solid state reactions using a modification of the Kissinger method. *J. Therm. Anal.* **1978**, *13*, 283–292. [[CrossRef](#)]
33. Malek, J. Kinetic analysis of crystallization processes in amorphous materials. *Thermochim. Acta* **2000**, *355*, 239–253. [[CrossRef](#)]
34. Málek, J.; Mitsuhashi, T. Testing method for the Johnson-Mehl-Avrami equation in kinetic analysis of crystallization processes. *J. Am. Ceram. Society* **2004**, *83*, 2103–2105. [[CrossRef](#)]
35. Lara, C.; Pascual, M.J.; Durán, A. Glass-forming ability, sinterability and thermal properties in the systems RO-BaO-SiO<sub>2</sub> (R = Mg, Zn). *J. Non Cryst. Solids* **2004**, *348*, 149–155. [[CrossRef](#)]
36. Hrubý, A. Evaluation of glass-forming tendency by means of DTA. *Czechoslov. J. Phys.* **1972**, *22*, 1187–1193. [[CrossRef](#)]
37. Baino, F.; Ferraris, M.; Bretcanu, O.; Verné, E.; Vitale-Brovarone, C. Optimization of composition, structure and mechanical strength of bioactive 3-D glass-ceramic scaffolds for bone substitution. *J. Biomater. Appl.* **2013**, *27*, 872–890. [[CrossRef](#)]
38. Massera, J.; Mayran, M.; Rocherullé, J.; Hupa, L. Crystallization behavior of phosphate glasses and its impact on the glasses' bioactivity. *J. Mater. Sci.* **2015**, *50*, 3091–3102. [[CrossRef](#)]
39. Gotor, F.J.; Criado, J.M.; Málek, J. Limitations of the Augis and Bennett Method for Kinetic Analysis of the Crystallization of Glasses and Conditions for Correct Use. *J. Am. Ceram. Soc.* **2001**, *84*, 1797–1802. [[CrossRef](#)]
40. Joraid, A.A. Limitation of the Johnson–Mehl–Avrami (JMA) formula for kinetic analysis of the crystallization of a chalcogenide glass. *Thermochim. Acta* **2005**, *436*, 78–82. [[CrossRef](#)]
41. Moharramand, A.H.; Rasheddy, M.S. A Simple Method for Crystallization Kinetics Determination and Its Application to Ge<sub>10</sub>Te<sub>35</sub>As<sub>55</sub> Glass. *Phys. Status Solidi (A)* **1998**, *169*, 33–41. [[CrossRef](#)]
42. Păcurariu, C.; Lazău, R.I.; Lazău, I.; Tița, D. Kinetics of non-isothermal crystallization of some glass-ceramics based on basalt. *J. Therm. Anal. Calorim.* **2007**, *88*, 647–652. [[CrossRef](#)]
43. Ray, C.S.; Day, D.E. Identifying internal and surface crystallization by differential thermal analysis for the glass-to-crystal transformations. *Thermochim. Acta* **1996**, *280–281*, 163–174. [[CrossRef](#)]
44. Agathopoulos, S.; Tulyaganov, D.U. Bioglasses and Glass-Ceramics in the Na<sub>2</sub>O-CaO-MgO-SiO<sub>2</sub>-P<sub>2</sub>O<sub>5</sub>-CaF<sub>2</sub> System. In *Bioceramics and Biocomposites: From Research to Clinical Practice*; Wiley Online Library: Hoboken, NJ, USA, 2019; pp. 123–148. [[CrossRef](#)]

**Disclaimer/Publisher's Note:** The statements, opinions and data contained in all publications are solely those of the individual author(s) and contributor(s) and not of MDPI and/or the editor(s). MDPI and/or the editor(s) disclaim responsibility for any injury to people or property resulting from any ideas, methods, instructions or products referred to in the content.